IEEE Journal of Microwaves

Received 11 February 2024; revised 14 June 2024 and 29 September 2024; accepted 4 December 2024.
Date of current version 9 January 2025.

*Digital Object Identifier 10.1109/JMW.2024.3516476*

# TX to RX Compact Leakage Cancellation Impedance Tuner for 60 GHz Monostatic Doppler Radar

**AHMAD MUSHTAQ [1], THOMAS MAUSOLF [2], WOLFGANG MIESCH [1], NASIR UDDIN [1] (Member, IEEE), WOLFGANG WINKLER [1] (Member, IEEE), AND DIETMAR KISSINGER [3] (Fellow, IEEE)**

*(Regular Paper)*

[1] Indie Semiconductor, 15236 Frankfurt, Germany
[2] IHP, Circuit Design Department, 15236 Frankfurt, Germany
[3] Institute of Electronic Devices and Circuits, Ulm University, 89069 Ulm, Germany

CORRESPONDING AUTHOR: Ahmad Mushtaq (e-mail: ahmad.mushtaq@indiesemi.com).

This work was supported by the German Federal Ministry of Education and Research under Grant BMBF FKZ: 13GW 0295.

**ABSTRACT** Monostatic radar shares a single antenna between the transmitter (TX) and receiver (RX) and offers an advantage of the reduced sensor size. However, due to the limited isolation of the coupler, the TX signal leaking into the RX significantly degrades the performance of the monostatic doppler radar. This paper presents the design of an ultra-compact impedance tuner (IT) which is connected to the lumped Rat-Race coupler to minimize the TX to RX leakage signal. The IT offers 5-bit phase control and 8-bit magnitude control via the Serial Peripheral Interface (SPI); moreover, it uses SiGe transistors in reverse saturation to enhance the impedance tuning performance. The size of the IT is only 0.04 mm$^2$ and its power consumption is 4 mW at 3.3V power supply. A two-channel 60 GHz monostatic doppler phased array radar chip has been designed and fabricated in 130 nm SiGe BiCMOS technology for vital signs monitoring application. The measured TX to RX isolation due to the Rat-Race coupler is 22 dB; moreover, IT provides the additional isolation of 27 dB, giving total TX to RX isolation of 49 dB at 60 GHz. The design, simulation and measurements of the IT and its measured leakage cancellation performance is reported in this paper.

**INDEX TERMS** Doppler radar, flicker noise, impedance tuner, leakage cancellation, monostatic radar, phased array radar, vector modulator, vital signs.

## I. INTRODUCTION

Continuous Wave Doppler Radar (CWDR) has a simple architecture, high sensitivity and is a preferred choice for the applications where only a small relative displacement of the target needs to be measured i.e., human chest motion due to cardiorespiratory activity [1]. In addition to the respiration and heartbeat rate measurements of the person via CWDR; it is very desirable to measure the heart sound to recognize the R-wave and T-wave as measured in the ECG signals [2]. This gives better estimation of the person's heart rate variability and can be used in the early diagnosis i.e. to detect the obstructive sleep apnea in the non-contact fashion during the sleep. The chest motion because of the respiration and the heartbeat is approximately 1 cm and 1 mm respectively but the heart sound generates the chest motion which is typically less than 30 $\mu$m [2]. That's why the detection of the heart sound requires a very sensitive radar. The high sensitivity in the CWDR to detect the heart sound is achieved via high gain LNA to suppress the mixer flicker noise and a high gain antenna to focus the beam precisely on the human torso. For practical reasons, the antenna beam should be steerable to adapt according to the different human body positions in the long-term vital sign monitoring e.g. over the night vital sign monitoring when the subject is sleeping. This can be achieved via the phased array radar. To reduce the number of antennas and the sensor size; a monostatic solution is desirable. In monostatic radar, transmitter (TX) and receiver (RX) share a single antenna and

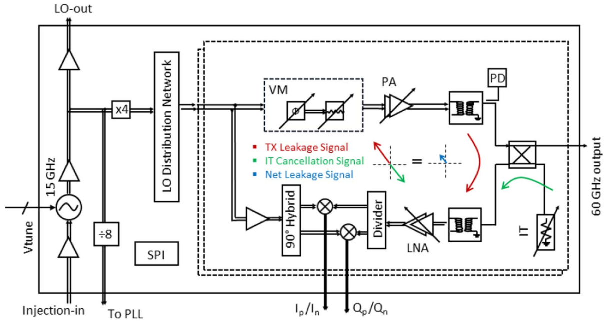


**FIGURE 1. Monostatic phased array doppler radar IC block diagram. Impedance Tuner (IT) is connected to the 4-port coupler and acts as leakage cancellation circuitry (LCC).**

isolation between them is provided via a coupler, as shown in the Fig. 1. However, integrated coupler provides limited isolation which leads to the problem of TX to RX leakage. In the presence of a high gain LNA, the TX leakage signal saturates the receiver degrading the signal to noise ratio (SNR) significantly.

Significant research work has been published in the last decade to solve the problem of TX to RX leakage or self-interference by integrating a leakage cancellation circuitry (LCC) on the chip [3]. If the *TX leakage signal* is $A_L cos(2\pi ft + \theta)$, the goal of LCC is to generate a *leakage cancellation signal* of the same amplitude but the opposite phase $A_L cos(2\pi ft + \theta + \pi)$ and add it to the TX leakage signal at the RX input. In this way, the *net leakage signal* is ideally zero, as shown in Fig. 1. Thus, the function of LCC is to provide additional TX to RX isolation on top of the limited coupler isolation. This additional isolation provided by LCC is called *leakage cancellation depth* (LC depth). In [4], [5], [6]; LCC consists of a variable gain amplifier (VGA), a variable phase shifter (VPS) and two couplers. A small amount of TX signal is coupled via the first coupler; its amplitude and phase are varied by the VGA and VPS respectively to get the desired leakage cancellation signal; and finally, the signal is coupled at the RX input via the second coupler to get ideally zero net leakage signal. In [7], [8], [9]; a similar topology is used as LCC; however, VGA and VPS are replaced with a Vector Modulator (VM) or In-phase Quadrature (IQ) Modulator. On the one hand, VGA and VPS based or VM based LCC topology is not compact and takes large chip area; and, on the other hand it also increases the power consumption of the chip. In multi-channel radar system, each channel requires its own LCC, exacerbating the problem of chip area and power consumption. In [10], a compact digital Impedance Tuner (IT) is used as LCC along with Quasi Circulator (QC). The designed QC provides good isolation if the digital IT is tuned to provide the same impedance as seen by the QC output port i.e. impedance of the antenna. This LCC topology is very compact and has negligible power consumption; however, leakage cancellation depth is limited because digital IT only provides 3.3-bit phase resolution (10 phase states) and 2-bit magnitude resolution. To overcome the limited resolution of digital IT, advance algorithm for controlling the digital IT is used in the paper [11] with good leakage cancellation results.

In this work, to connect the TX and RX to a single antenna, a compact lumped 4-port Rat-Race coupler has been used with one port terminated with compact high-resolution IT as shown in Fig. 1. IT acts as LCC and magnitude and phase of the IT can be controlled via the SPI interface with 8-bit and 5-bit resolution respectively. The part of TX signal reflected from the IT generates the leakage cancellation signal, which adds vectorially to the TX leakage signal at the RX input and provides the opportunity to cancel the TX leakage signal via destructive interference. The paper is organized as follows. Section II briefly describes the chip architecture and SNR improvement possibility because of LCC. Section III explains the design, analysis and simulation results of the IT. In Section IV, measured leakage cancellation performance of the IT is described. Conclusions are presented in Section V.

## II. CHIP ARCHITECTURE

Fig. 1 shows the block diagram of the two-channel 60 GHz monostatic phased array radar IC. The TX path of each channel consists of a vector modulator (VM) and a power amplifier (PA). VM enables the beam steering capability in the TX mode and controls the TX output power. RX path consists of high gain LNA and IQ receiver. Beam steering in the RX path is achieved via digital beamforming. The TX to RX isolation is provided via a compact single transformer based lumped Rat-Race coupler [12]. Integrated coupler can only offer limited isolation between the TX and RX. Moreover bond-wire or package inductance and non-ideal 50 Ω antenna impedance at the coupler output port exacerbates the problem at hand. To mitigate the TX leakage into RX, IT is connected at the coupled port of the 4-port coupler; and, controlled via the SPI interface to generate the leakage cancellation signal at the RX input. Additionally, the chip integrates an injection lock oscillator so that multiple chips can be cascaded, if required, to increase the number of channels in the phased array operation [13]. Fig. 2 shows the chip photograph fabricated in 130 nm SiGe BiCMOS technology. The compact 1-D geometry of IT is easily placed between the TX and RX of each monostatic radar channel. Fig. 3 shows the IT block diagram. The IT has a single port ($P_{IT}$) which is connected to the coupler port $P3$. The IT concept will be explained in detail in Section III.

The vital sign signals i.e. heart beat and heart sound are very low frequency signals and located very close to DC in the CWDR receiver output. In our application, the chosen bandwidth of interest for the detection of the heart sound is 1 Hz–100 Hz. The low frequency spectrum at the receiver output is dominated by the mixer flicker noise and its rms value is given by (2).

$$v_{n-total} = \sqrt{v_{f-mixer}^2 + v_{th-mixer}^2 + v_{th-LNA}^2} \qquad (1)$$

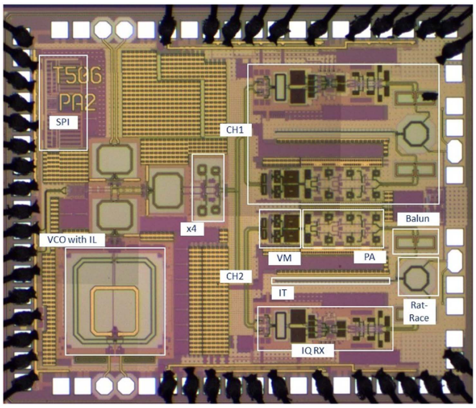


**FIGURE 2.** Two-channel 60 GHz phased array doppler radar chip with LCC. Chip size: 2.1 mm x 1.8 mm.

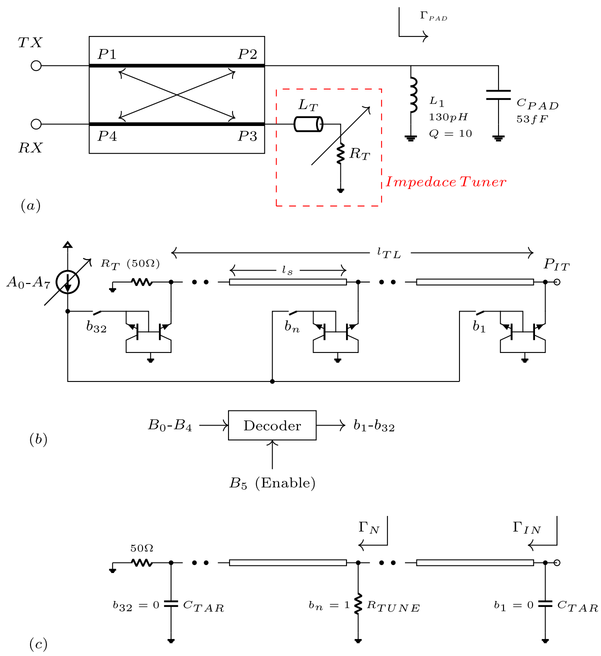


**FIGURE 3.** (a) IT connected to the coupled port. (b) Simplified block diagram of IT. (c) Equivalent model when TARn is active.

$$v_{f-mixer} = e_{nf}\sqrt{\ln\left[\frac{f_H}{f_L}\right]} \tag{2}$$

$$v_{th-mixer} = NF_{mixer}\, G_{mixer}\sqrt{KTR(f_H - f_L)}$$

$$v_{th-LNA} = NF_{LNA}\, G_{LNA}\, G_{mixer}\sqrt{KTR(f_H - f_L)}$$

$$|IS_{coupler}| \geq PA_{out} + G_{LNA} - IP_{1dB-mixer}$$

$$|IS_{coupler}| \geq 10\, dB + G_{LNA} \tag{3}$$

$e_{nf} = 1.1\ uV$ is the normalized flicker noise at 1 Hz output frequency, $f_H = 100$ Hz and $f_L = 1$ Hz are the upper and lower limits of the frequency region of the interest. The total rms noise voltage at the receiver output $v_{n-total}$ can be written as (1). $v_{th-LNA}$ and $v_{th-mixer}$ give rms noise contribution

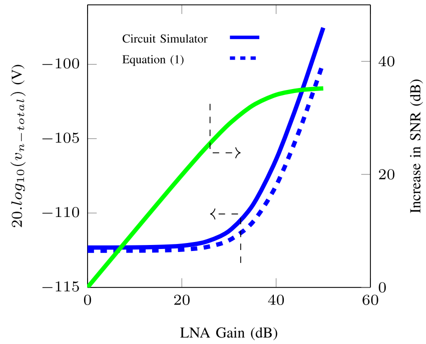


**FIGURE 4.** Receiver output RMS noise within the bandwidth 1 Hz- 100Hz and increase in the SNR with respect to the LNA Gain.

at the receiver output due to the LNA and mixer thermal noise respectively. $K$ is the Boltzmann constant, $T$ is the temperature in Kelvin, $R = 50\ \Omega$ is the input resistance of the LNA and mixer, $NF_{LNA} = 5.5$ dB is the noise figure of the LNA, $NF_{mixer} = 15.5$ dB is the noise figure of the mixer considering only its thermal noise, $G_{mixer} = 10$ dB and $G_{LNA}$ is the mixer voltage conversion gain and LNA gain respectively. In the desired bandwidth $f_L$ to $f_H$, mixer flicker noise dominates and total rms noise $v_{n-total} \approx v_{f-mixer}$. Mixer thermal noise $v_{th-mixer}$ is orders of magnitude lower than $v_{f-mixer}$ whereas $v_{th-LNA}$ depends on the LNA gain. Fig. 4 plots the $v_{n-total}$ from (1) with respect to the LNA gain. For a comparison purpose, $v_{n-total}$ at the receiver output is also directly simulated with the help of a commercial circuit simulator and plotted in the same graph. It can be seen that $v_{n-total}$ stays almost constant till the LNA gain is increased to 30 dB. Since the output signal power increases linearly with respect to the LNA gain, the SNR of the output signal also increases linearly with the LNA gain till $v_{th-LNA}$ becomes comparable to $v_{f-mixer}$. Therefore, the high gain LNA can be used to suppress the effect of the mixer flicker noise and increases the SNR of the CWDR significantly for the vital sign detection applications.

However, the TX power leaking to RX is amplified by the LNA gain and can saturate the mixer; so, high gain LNA demands better coupler isolation ( $IS_{coupler}$) given by (3). $PA_{out} = 10$ dBm is the PA output power and $IP_{1dB-mixer} = 0$ dBm is mixer input 1 dB compression point. Integrated couplers in the mm-wave frequency range offer limited isolation of 15–20 dB in the presence of bond-wire and non-ideal 50 Ω antenna impedance thus limiting the gain of the LNA to approximately 10 dB. To increase the SNR by using high gain LNA, it is required to increase the coupler isolation. For 30 dB LNA gain, the coupler isolation $IS_{coupler}$ should be more than 40 dB. This is achieved by the addition of the impedance tuner at the coupled port of the 4-port coupler.

## III. DESIGN AND ANALYSIS OF IMPEDANCE TUNER

### A. CONCEPT

The concept of IT is shown in Fig. 3. The IT consists of a high impedance transmission line (TL) of length $l_{TL}$ with $L_{TL}$

inductance per meter and $C_{TL}$ capacitance per meter [11]. The TL is divided into $n_{max} = 31$ equal length sections each having length of $l_s$. A high quality *tunable active resistor* (TAR) consisting of SiGe HBTs is connected at the beginning of each TL section. The TL is terminated with $R_T$ (50 Ω) resistor in parallel with an additional TAR. The TAR-n $(0 \leq n \leq n_{max}+1)$ can be turned on/off digitally via SPI by controlling the bit $b_n$. At any given time, maximum one TAR is allowed to turn on via 5-32 bit digital decoder. Here $n = 0$ implies that no TAR cell is active and this is done via the enable pin of the 5-32 bit decoder i.e. $B5$ in Fig. 3(b). In the ON-state TAR can be modelled as a resistor $R_{TUNE}$ and in the OFF-state as a capacitor $C_{TAR}$ as shown in the Fig. 3(c). The resistance value of TAR in the on-state $R_{TUNE}$ is controlled by 8-bit ( $A_0 - A_7$) bias current control via SPI. The characteristic impedance $Z_0$ of high impedance TL in the presence of connected TAR cells is given by (4). The parameters are chosen such that $Z_0 = 50\ \Omega$. To drive the expression of reflection coefficient $\Gamma_{IN}$ at the input port of the IT, consider bit $b_n$ is active with TAR-n having resistance $R_{TUNE}$, as shown in Fig. 3(c). The reflection coefficient $\Gamma_{IN}$ is given by (5). The magnitude of $\Gamma_{IN}$ depends on $R_{TUNE}$, which can be controlled with 8-bit resolution via the SPI interface. Phase of $\Gamma_{IN}$ depends on the position of the active TAR-n along the TL. The phase resolution of the IT is given by $\frac{4\pi}{\lambda_E} l_s$ where $\lambda_E$ is the effective wavelength in the substrate considering the slow wave velocity due to $C_{TAR}$. Smaller the $l_s$, better would be the IT phase resolution. However, $l_s$ can't be made arbitrary small because of (4). For the TL parameters $L_{TL}$ and $C_{TL}$; the smaller the value of $C_{TAR}$, smaller is the value of $l_s$ and better is the IT phase resolution. Moreover, (6) should be satisfied to cover the full $360^\circ$ phase coverage with IT.

$$Z_0 = \sqrt{\frac{L_{TL}}{C_{TL} + C_{TAR}/l_s}} \tag{4}$$

$$\Gamma_{IN} = \Gamma_N\, e^{-j\frac{4\pi}{\lambda_E}(n-1)l_s} \qquad (1 \leq n \leq n_{max}+1) \tag{5}$$

$$\Gamma_{IN} = 0 \qquad (n = 0)$$

$$\Gamma_N = \frac{(Z_0||R_{TUNE}) - Z_0}{(Z_0||R_{TUNE}) + Z_0}$$

$$\frac{4\pi}{\lambda_E} n_{max} l_s = \frac{4\pi}{\lambda_E} l_{TL} \geq 2\pi \Rightarrow l_{TL} \geq \frac{\lambda_E}{2} \tag{6}$$

### B. DESIGN

The circuit concept was implemented and verified in the design of a 2-channel phased array radar transceiver. To satisfy (6), the length $l_{TL}$ of the transmission line in the design was chosen to be 527 µm and it is drawn on the top metal layer of thickness 3 µm to minimize the signal loss. Metal GND has not been drawn exactly below the TL but shifted 10 µm to a side; moreover, width of the TL was chosen 2.4 µm to maximize $L_{TL}$ and minimize $C_{TL}$ while maintaining good production yield for relatively long TL. The layout of the IT is shown in Fig. 5. The $L_{TL}$ and $C_{TL}$ values of the TL are 645 $nH/m$ and 135 $pF/m$ respectively and determined via the EM simulator.

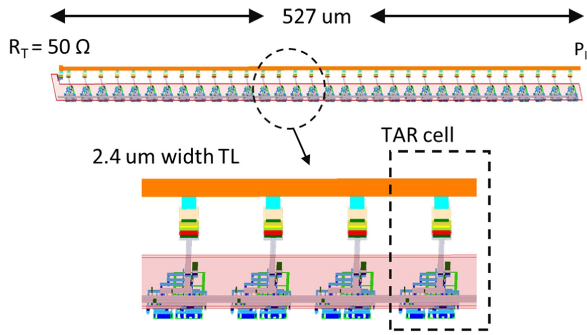


**FIGURE 5.** Layout view of the IT. 32 TAR cells are connected to a 527 $\mu$m long transmission line. Position of the active TARn (1:32) determines the phase, whereas resistance of the active TAR $R_{TUNE}$ determines the magnitude of the leakage cancellation signal. Position is controlled by 5-bit phase code ($B_0 - B_4$) and resistance is controlled by 8-bit magnitude code ($A_0 - A_7$) as shown in Fig. 3.

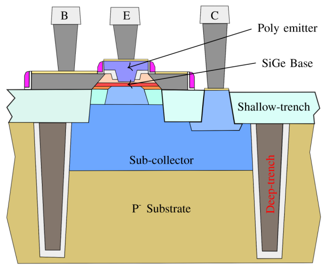


**FIGURE 6.** Device cross section of a SiGe HBT.

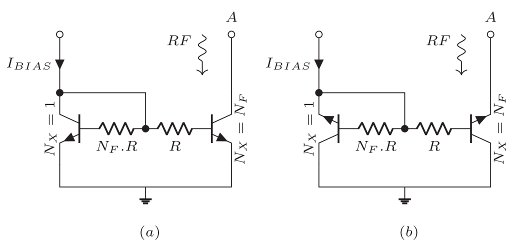


**FIGURE 7.** TAR cell configuration. (a) Standard. (b) Reverse Saturated.

Fig. 7(a) shows a standard configuration for implementing the TAR cell. The performance of this unit cell can be considerably increased if the emitter is connected to the RF port instead of the collector as shown in Fig. 7(b). This is because, the emitter in the HBT device is physically isolated from the p-substrate and offer much less capacitance but the n+ collector makes a pn junction with the substrate and offers relatively large capacitance. The cross section of a high speed SiGe HBT device is shown in Fig. 6 [14]. The topology is referred as *Reverse Saturated* configuration in the literature [15]. It is important to mention that in both configurations, node 'A' should be at DC ground potential which is achieved in this design by connecting coupler port 2 to GND via inductor $L_1$, see Fig. 3(a). Additionally, this inductor resonates with the pad capacitance at 60GHz and provides the bandpass response.

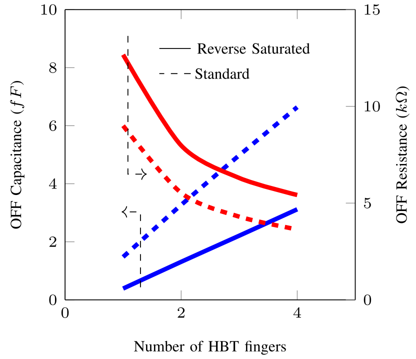


**FIGURE 8. Simulated comparison of OFF capacitance and OFF resistance between Standard and Reverse Saturated TAR configurations.**

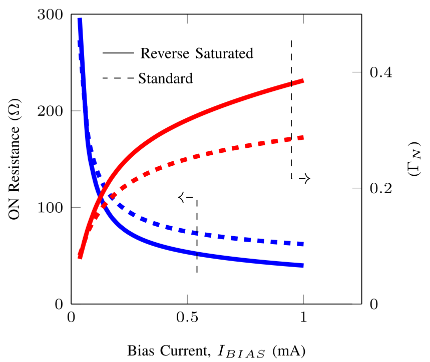


**FIGURE 9. Simulated ON resistance $R_{TUNE}$ and $\Gamma_N$ with respect to the bias current $I_{BIAS}$.**

Fig. 8 compares the *OFF Capacitance* and *OFF Resistance* (i.e., when bias current $I_{BIAS}$ is '0') of the two configurations. The capacitance offered by reverse saturated configuration is half than that of standard configuration. Moreover, it also offers advantage in terms of high OFF Resistance. To satisfy (4), TAR with 3 fingers HBT having $C_{TAR}$ value of $2\ fF$ has been used along with $l_s = 17\ um$. This provides the phase resolution of approximately $11^\circ$ at 60 GHz. Fig. 9 shows the $R_{TUNE}$ and $\Gamma_N$ with respect to the bias current $I_{BIAS}$ for 3 finger HBT ( $N_F = 3$) in standard and reverse saturated configurations. The reverse saturated configuration also has the advantage of lower *ON Resistance* $R_{TUNE}$; thus providing higher $|\Gamma_{IN}|$. The $S_{11}$ of the IT under different control conditions can be written as $(S_{11}^{\mathrm{IT}})^{\mathrm{P}}_{\mathrm{M}}$ where $M = 0:255$ is the 8-bit magnitude control and $P = 0:32$ is the 5-bit phase control. $M$ is controlled via the bias current $I_{BIAS}$ with SPI bits $A_0 - A_7$ whereas $P$ is controlled via SPI bits $B_0 - B_4$ as shown in Fig. 3(b). For the sake of completion, it is important to mention that the 5-32 bit decoder has an enable bit $B_5$. $P = 0$ is defined as when $B_5 = 0$. In this condition no TAR cell is active i.e. $(S_{11}^{\mathrm{IT}})^{\mathrm{P=0}}_{\mathrm{M}} = 0$ i.e. $50\ \Omega$ match via $R_T$. The $(S_{11}^{\mathrm{IT}})^{\mathrm{P}}_{\mathrm{M}}$ simulation results for different values of $M$ are shown in Fig. 21(a). Note that maximum $|\Gamma_{IN}|$ reduces with increasing $P$. This is because with increasing $P$, the active TAR-n cell is further way from the IT input port $P_{IT}$ and hence RF signal must travel larger distance to reflect from TAR cell increasing the two-way signal loss.

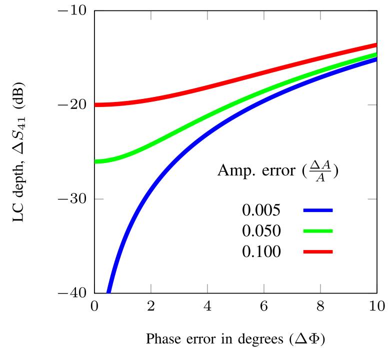


**FIGURE 10. Theoretical leakage cancellation depth with respect to phase error $\Delta\Phi$ and amplitude error $\frac{\Delta A}{A}$.**

### C. LEAKAGE CANCELLATION DEPTH

The Impedance Tuner has limited resolution i.e., 5-bit phase resolution and 8-bit magnitude resolution. Because of the limited resolution, the perfect leakage cancellation signal can not be produced under all conditions. In this sub-section, the possible worst-case leakage cancellation depth due to the limited IT resolution will be derived. If the TX leakage signal at RX input is **A** and imperfect leakage cancellation signal is **B** having $\Delta\phi$ phase error and $\Delta A$ amplitude error; then, the leakage cancellation depth $\Delta S(4, 1)$ (i.e., improvement in the coupler isolation) can be written as (7) [7] and plotted in Fig. 10. 5-bit phase resolution corresponds to approximately 11°phase step at 60 GHz. Hence, the maximum possible phase error $\Delta\phi_{max}$ will be 5.5°. The leakage signal amplitude A and leakage cancellation signal amplitudes B at RX input can be written as $A = S_{41}\ V_{PA}$ and $B = S_{31}\ S_{43}\ V_{PA}\ (S_{11}^{\mathrm{IT}})^{\mathrm{P}}_{\mathrm{M}}$ where $(S_{11}^{\mathrm{IT}})^{\mathrm{P}}_{\mathrm{M}}$ magnitude can be changed with 8-bit resolution. Using this information, maximum amplitude error $\frac{\Delta A}{A}$ can be calculated as (8). $V_{PA}$ is the PA output signal.

$$\Delta S(4, 1)_{,dB} = 10\ log_{10}\left\{1 - 2\left(1 + \frac{\Delta A}{A}\right) cos\Delta\phi + \left(1 + \frac{\Delta A}{A}\right)^2\right\} \tag{7}$$

$$\frac{\Delta A}{A} = \frac{S_{31}\ S_{43}\ V_{PA}\ (S_{11}^{IT})_{MAX}}{255\ S_{41}\ V_{PA}} \approx 0.006 \tag{8}$$

With 5-bit phase resolution and 8-bit magnitude resolution, the Impedance Tuner (IT) should provide $\approx$20 dB leakage cancellation depth in the worst case according to Fig. 10. Measured LC-depth with respect to frequency has been plotted in Fig. 19. The IT magnitude code ( $M$) and phase code ( $P$) have been set at each frequency point to provide the best possible LC-depth. The measurements are in good agreement with the theory. This is additional isolation provided by the IT

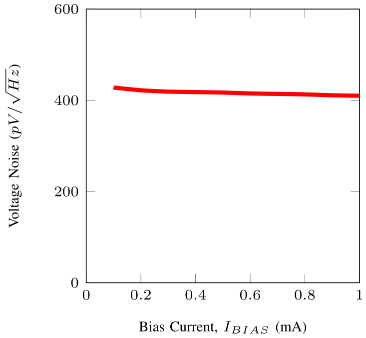


**FIGURE 11.** Simulated voltage noise density produced by IT (TAR cell parallel with $R_T = 50\ \Omega$) connected to a noiseless $50\ \Omega$ resistor (i.e. coupler port 3 impedance, Fig. 12(b).

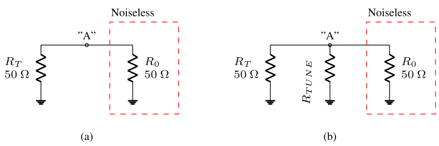


**FIGURE 12.** Simplified circuit for noise analysis. (a) IT is OFF. (b) IT is ON. TAR cell, modeled as $R_{Tune}$, produces shot noise.

because of the leakage cancellation on top of coupler own isolation.

### D. IMPEDANCE TUNER NOISE

The noise analysis has been detailed in the Section II. The IT cancels the TX leakage signal at RX input and increases the TX-to-RX isolation. This enables the use of high gain LNA to suppress the mixer flicker noise. However, the IT shouldn't increase the noise floor at the RX input by adding its own noise. Fig. 12(a) shows the simplified circuit when IT is off. Noiseless resistor $R_0 = 50\ \Omega$ models the Rat-Race coupler port 3 impedance whereas $R_T = 50\ \Omega$ is the termination resistor which generates the thermal noise of voltage density $\sqrt{4KTR_T}$. The voltage noise density at node "A", when IT is off, is equal to $\sqrt{KTR_T} = 450 pV/\sqrt{Hz}$ because of voltage division. Fig. 12(b) shows the simplified circuit when IT is on where TAR cell is modelled as $R_{TUNE}$. The voltage noise density at node "A" with respect to bias current $I_{BIAS}$ is plotted in Fig. 11 from the circuit simulator. It should be noted that the voltage noise density is almost the same as it is when the IT is switched off i.e., $450 pV/\sqrt{Hz}$. Analytically, there are now two dominant sources contributing noise at node "A". The voltage noise density due to $R_T$ is $\bar{v_1}$ given by (9). The second noise source is TAR cell which is modelled as $R_{TUNE}$. Since, node "A" is also at DC GND, base-emitter and base-collector junctions are forward biased when $I_{BIAS}$ is applied; giving equivalent $R_{TUNE}$ resistor as a function of $I_{BIAS}$. The voltage noise density due to $R_{TUNE}$ is $\bar{v_2}$ given by (10). $I_b$ is the base current and $q$ is the the charge of electron. The total noise at node "A" is given by $\bar{v_t} = \sqrt{\bar{v_1}^2 + \bar{v_2}^2}$. For $I_{BIAS} = 1\ mA$, the values of $I_b$ is $250\ uA$ and $\bar{v_t} = 340\ pV/\sqrt{Hz}$. To sum up, IT doesn't increase noise floor at the RX input by adding its own noise.

$$\bar{v_1} = \sqrt{4KTR_T}\,\frac{R_{TUNE}||R_0}{(R_{TUNE}||R_0) + R_T} \tag{9}$$

$$\bar{v_2} = \sqrt{2q\,I_b}\,.\,(R_0||R_{TUNE}||R_T) \tag{10}$$

**TABLE 1.** Important TRX Parameters

| Parameter | Value |
|---|---|
| LNA Gain ($G_{LNA}$) | 20 $dB$ |
| Mixer Gain ($G_{MIXER}$) | 10 $dB$ |
| RX Gain ($G_{RX}$) | 30 $dB$ |
| LNA Noise Figure ($NF_{LNA}$) | 5.5 $dB$ |
| Mixer Noise Figure ($NF_{mixer}$) | 15.5 $dB$ |
| RX Input 1dB Point ($IP_{1dB}$) | -20 $dBm$ |
| PA Output Power ($P_{PA}$) | Fig. 13 |

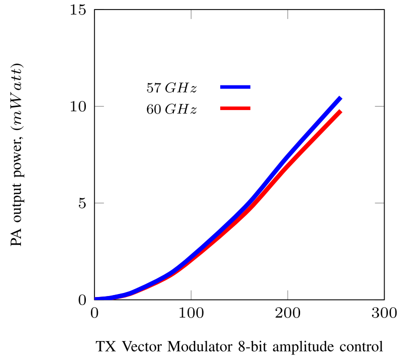


**FIGURE 13.** PA output power control with TX vector modulator. The power is measured at chip output Pad. The coupler insertion loss $|S(2,1)| = 5.5$ dB is compensated to calculate the PA output power.

## IV. MEASUREMENT RESULTS

Four different types of measurements are performed to validate the IT design. In the first measurement, the TX to RX leakage cancellation capability of the IT is measured. It was concluded that IT reduces the TX leakage signal by 27 dB at 60 GHz. In the second measurement, $(S_{11}^{\mathrm{IT}})_{\mathrm{M}}^{\mathrm{P}}$ of the IT is indirectly measured at RX output and compared with the simulation results at 60 GHz. In the third measurement, an external signal of 60 GHz is provided as input to the chip and RX IQ diagram is measured under three different cases 1) when the TX is off and there is no TX leakage signal to degrade the RX performance 2) when the TX is on 3) when the TX is on, and IT is configured to cancel the TX leakage signal. A preliminary radar prototype is designed with the RF chips wire-bonded on a RF board with 60 GHz antennas to further validate the efficacy of the IT to mitigate the performance degradation caused by TX to RX leakage.

Important transceiver parameters are given in Table 1. Fig. 13 shows the measured PA output power control done by the Vector Modulator (VM) in the TX path. For different IT measurements, PA output power is set at different levels in order not to saturate the RX and to operate it in the linear region. Moreover, IQ RX has 1.8 dB and 7 ° magnitude and phase imbalance respectively at 60 GHz, which is calibrated for the measurements of the IT.

### A. MEASURED TX TO RX LEAKAGE CANCELLATION

The TX leakage signal generates the DC offset in the IQ receiver due to self-mixing with LO. If the RX is operating in the linear region, the DC magnitude of the IQ vector at RX output will be directly proportional to the net leakage power at RX input. The *net leakage signal* at RX input is the vector sum of the *TX leakage signal* and *IT leakage cancellation signal*. The net leakage signal at RX input can be written as $(A_L)^P_M\, cos(2\pi\ f_{TX}\ t + \phi^P_M)$, where $P$ and $M$ are the IT phase and magnitude code respectively, $f_{TX}$ is the frequency of operation i.e. 60 GHz and $(A_L)^P_M$ is the amplitude of the net leakage signal at the RX input. Only considering the low frequency component (low pass filter response), the IQ vector at RX output $\vec{\Lambda}^P_M$ can be written as (11).

$$\overrightarrow{\Lambda^P_M} = \Delta I^P_M + j\Delta Q^P_M = |\vec{\Lambda}^P_M|\ \angle\theta^P_M \tag{11}$$

$$\Delta I^P_M = (I_p)^P_M - (I_n)^P_M$$

$$\Delta Q^P_M = (Q_p)^P_M - (Q_n)^P_M$$

$$|\vec{\Lambda}^P_M| = \sqrt{(\Delta I^P_M)^2 + (\Delta Q^P_M)^2} = (A_L)^P_M G_{RX} \tag{12}$$

$$\angle\theta^P_M = \tan^{-1}\left(\Delta Q^P_M/\Delta I^P_M\right)$$

$$\overrightarrow{\Delta^P_M} = \overrightarrow{\Lambda^P_M} - \overrightarrow{\Lambda^P_M}|_{M=0\vee P=0} \tag{13}$$

$$\Delta S(4,1) = 20\ log_{10}\left[\frac{|\overrightarrow{\Lambda^P_M}|}{|\overrightarrow{\Lambda^P_M}||_{M=0\vee P=0}}\right] \tag{14}$$

$\Delta I^P_M$ and $\Delta Q^P_M$ are the differential In-phase and Quadrature signals at the RX output, which are measured for different $M$ and $P$ settings of the IT. $|\vec{\Lambda}^P_M|$ is directly proportional to $(A_L)^P_M$ according to (12) where $G_{RX} = G_{LNA}.G_{MIXER}$ is the voltage conversion gain of the RX. Therefore the objective of the IT is to minimize $|\vec{\Lambda}^P_M|$ by adjusting $P$ and $M$. $\overrightarrow{\Lambda^P_M}|_{M=0\vee P=0}$ (when either $M$ or $P$ is zero) gives the IQ vector response only due to TX leakage signal since IT cancellation signal is zero in this case. IT cancellation signal $\overrightarrow{\Delta^P_M}$ can be calculated mathematically as (13).

The measured vectors at RX output $\overrightarrow{\Lambda^P_M}|_{M=0\vee P=0}$, $\overrightarrow{\Lambda^P_M}$ and $\overrightarrow{\Delta^P_M}$ are shown in the Fig. 14 at 60 GHz. In this measurement, the coupler port 2 or chip output pad (Fig. 3(a)) is connected to the 67 GHz Spectrum Analyser *R&S FSW67* via Ground-Signal-Ground (G-S-G) probe. This provides the 50 Ω load or termination at the chip output pad. In order not to saturate the RX section, PA power is configured at −2 dBm via controlling the vector modulator in the TX chain as shown in Fig. 13. The TX leakage signal at RX input can be calculated as: $(A_L)^P_M|_{M=0\vee P=0} = |\overrightarrow{\Lambda^P_M}||_{M=0\vee P=0}/G_{RX} =$

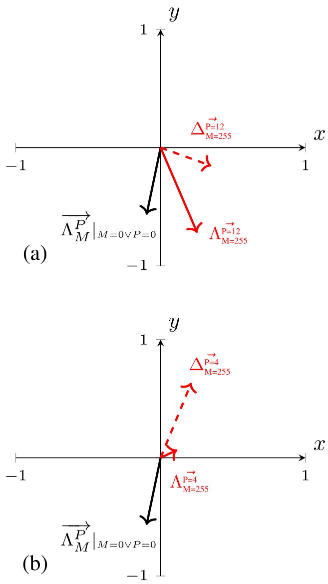


**FIGURE 14.** Measured IQ vectors. 1) $\vec{\Lambda}^P_M$ is the vector due to the ***net leakage signal*** at RX input. 2) $\vec{\Lambda}^P_M|_{M=0\vee P=0}$ is the vector due to only ***TX leakage signal*** at RX input because IT is off in this case. 3) $\vec{\Delta}^P_M$ is the vector due to only ***IT leakage cancellation signal*** and calculated from (13).

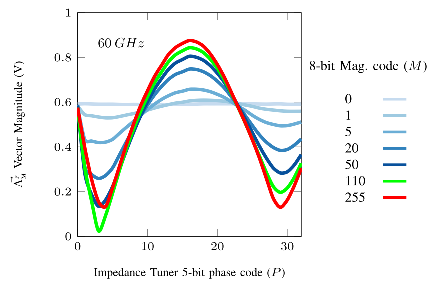


**FIGURE 15.** Measured $\vec{\Lambda}^P_M$ vector magnitude w.r.t. Impedance Tuner 5-bit phase code $\mathbf{P = 0:32}$ for different Impedance Tuner magnitude codes $\mathbf{M = 0, 1, 5, 20, 50, 110, 255}$.

$0.6V/31.6 = 19mV$ or equivalently $-24$ dBm in 50 Ω system. Knowing the PA output power and TX leakage signal at RX input, coupler own isolation $S(4,1)$, when IT is off ($M = 0 \vee P = 0$), comes out to be $-24 - (-2) = -22$ dB at 60 GHz.

The net leakage signal at RX input $(A_L)^P_M$ is directly proportional to $|\overrightarrow{\Lambda^P_M}|$ according to (12). The measured $|\overrightarrow{\Lambda^P_M}|$ at 60 GHz is shown in the Fig. 15 with respect to $P = 0:32$ and several values of $M$. The leakage cancellation depth due to IT or the increase in the coupler isolation $\Delta S(4,1)$ only because of the IT can be calculated from (14) and results are plotted in Figs. 16 and 17. The coupler achieves 27 dB isolation improvement at $M = 110$ and $P = 4$ at 60 GHz. Here it is important to mention that this is additional isolation due to the IT leakage cancellation circuitry on top of the coupler own isolation of 22 dB at 60 GHz. Fig. 18 shows the measured LC depth with respect to the PA output power at 60 GHz and Fig. 19 shows the LC depth achieved at different frequencies

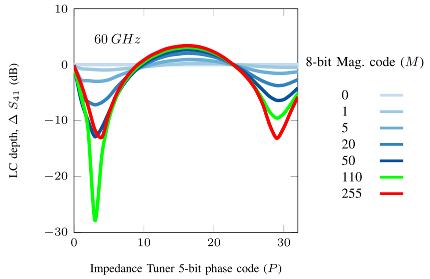


**FIGURE 16.** Measured change in TX-RX Isolation ($\Delta S_{41}$) w.r.t. Impedance Tuner 5-bit phase code $\mathbf{P} = \mathbf{0}:\mathbf{32}$ for different Impedance Tuner magnitude codes $\mathbf{M} = \mathbf{0}, \mathbf{1}, \mathbf{5}, \mathbf{20}, \mathbf{50}, \mathbf{110}, \mathbf{255}$. The Isolation improves by 27 dB at 60 GHz for $\mathbf{M} = \mathbf{110}$ and $\mathbf{P} = \mathbf{4}$.

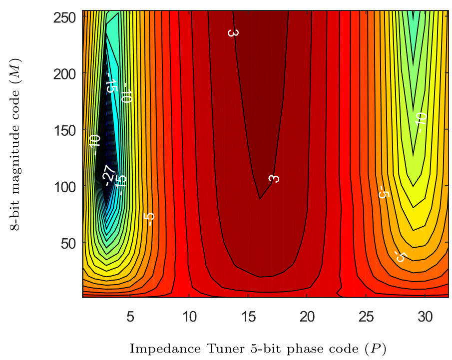


**FIGURE 17.** Measured LC depth or change in TX-RX Isolation $\Delta S(4, 1)$ dB because of IT at 60 GHz by adjusting the IT phase (P) and magnitude code (M). To reduce measurement time, M is adjusted only in coarse steps of 10 when $\mathbf{M} > \mathbf{10}$.

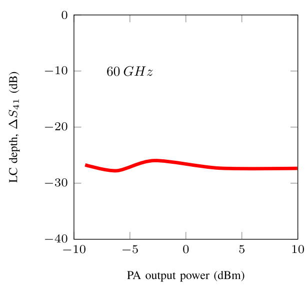


**FIGURE 18.** Measured LC depth with respect to PA output power.

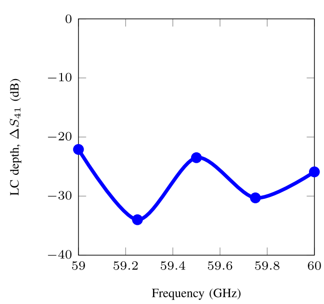


**FIGURE 19.** Measured LC-Depth (dB) with respect to the frequency. IT phase code (*P*) and magnitude code (*M*) have been adjusted at each frequency point to provide the best possible leakage cancellation.

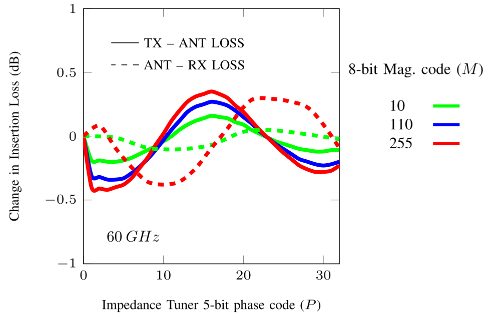


**FIGURE 20.** Measured change in TX-ANT Insertion Loss ($\Delta S_{21}$) and ANT-RX Insertion Loss ($\Delta S_{42}$) w.r.t. Impedance Tuner 5-bit phase code $\mathbf{P} = \mathbf{0}:\mathbf{32}$ for different Impedance Tuner magnitude codes $\mathbf{M} = \mathbf{10}, \mathbf{110}, \mathbf{255}$.

from 59 GHz to 60 GHz. Due to discrete nature of phase and magnitude steps of leakage cancellation signal, the LC depth is best achieved at certain frequencies when the phase is close to the ideal required phase. However, as analysed in the Section III-C, the worst case LC depth with 5-bit phase resolution and 8-bit magnitude resolution is better than 20 dB. Fig. 20 shows the measured change in TX-to-Ant insertion loss and Ant-to-RX insertion loss when IT phase code $P$ is varied at different magnitude codes $M$. The insertion loss only changes by $\pm 0.5$ dB maximum whereas the TX-RX Isolation can be improved by 27 dB at 60 GHz and 35 dB at 59.2 GHz.

### B. MEASURED $S_{11}$ OF THE IT

To measure the $S_{11}^{IT}$ of the IT, output power of the PA output signal $V_{PA}\, e^{j\Theta_{PA}}$ is configured $-13$ dBm by controlling the vector modulator in the TX path. Moreover coupler port 2 or chip output pad (Fig. 3(a)) is left open in this measurement. $L_1$ resonates with $C_{PAD}$ at 60 GHz and $\Gamma_{PAD} \approx 0.8$. Under these conditions, RX output IQ vectors due to the TX leakage signal $\overrightarrow{\Lambda_M^P}|_{M=0 \vee P=0}$ and leakage cancellation signal $\overrightarrow{\Delta_M^P}$ can be written as (15) and (16) respectively considering $S_{41} << S_{21} S_{42} \Gamma_{PAD}$, where $S_{xy}$ is the S parameter of the coupler as shown in Fig. 3(a).

$$\overrightarrow{\Lambda_M^P}|_{M=0 \vee P=0} = |V_{PA}|\, e^{j\Theta_1}\, S_{21}\, S_{42}\, \Gamma_{PAD}\, G_{RX} \tag{15}$$

$$\text{where} \quad \Theta_1 = \angle S_{21} + \angle S_{42} + \angle G_{RX} + \Theta_{PA}$$

$$\overrightarrow{\Delta_M^P} = -|V_{PA}|\, e^{j\Theta_1}\, S_{21}\, S_{42}\, (S_{11}^{\mathrm{IT}})_{\mathrm{M}}^{\mathrm{P}}\, G_{RX}$$

$$\because\; S_{31}\, S_{43} = -\, S_{21}\, S_{42} \tag{16}$$

$$|(S_{11}^{\mathrm{IT}})_{\mathrm{M}}^{\mathrm{P}}| = \left( \frac{|\overrightarrow{\Delta_M^P}|}{|\overrightarrow{\Lambda_M^P}|_{M=0 \vee P=0}|} \right) \Gamma_{PAD} \tag{17}$$

$$\angle\left((S_{11}^{\mathrm{IT}})_{\mathrm{M}}^{\mathrm{P}}\right) = \angle(\overrightarrow{\Delta_M^P}) - \pi - \Theta_1 \quad \text{where } \Theta_1$$

$$= \angle\left(\overrightarrow{\Lambda_M^P}|_{M=0 \vee P=0}\right) \tag{18}$$

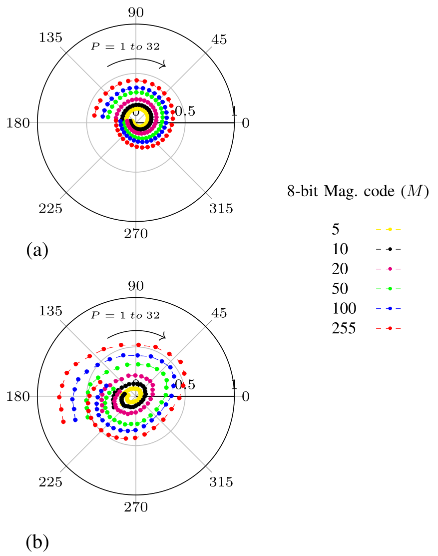


**FIGURE 21.** (a) Simulated S-Parameters ($S_{11}{}_M^{P=1:32}$) of the Impedance Tuner. (b) Indirectly measured S-Parameter of the Impedance Tuner.

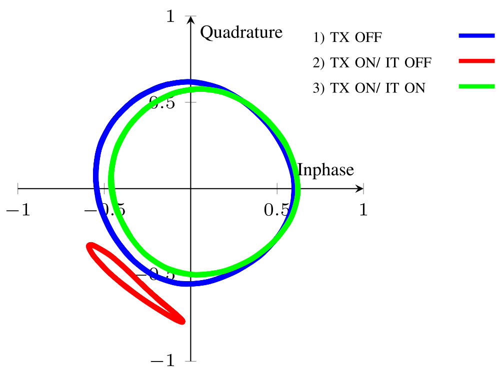


**FIGURE 22.** Measured RX IQ diagram for three different cases. 1) TX is off, 2) TX is ON but Impedance Tuner is off. 3) TX leakage signal cancelled via Impedance Tuner.

Equations (17) and (18) gives magnitude and angle of the $(S_{11}^{\mathrm{IT}})_{\mathrm{M}}^{\mathrm{P}}$ respectively. Simulation and measurement results of $(S_{11}^{\mathrm{IT}})_{\mathrm{M}}^{\mathrm{P}}$ are plotted in Fig. 21.

### C. MEASURED RX IQ DIAGRAM

In this measurement, the LO frequency is set at $f_{TX} =$ 60 GHz and an external sinusoidal signal of frequency $f_{TX} + \delta_f$ is provided at the chip output pad via G-S-G probe. The external signal is generated via *R&S SMA100B* signal generator. The RX differential In-phase signal $\Delta I$ and differential Quadrature signal $\Delta Q$ are sampled via the Digital Oscilloscope. IQ diagram is plotted in Fig. 22 for three different cases. In the first case, the TX is completely turned off. In this case, there would be no TX leakage signal into the receiver and the RX performance will not be degraded by the TX leakage signal. In the second case, the TX is on and vector modulator in the TX path is configured such that PA output power is 5 dBm. IT is off in the second case i.e. $M = 0 \vee P = 0$. It can be seen that IQ digram is completely distorted because of the TX leakage signal. The third case is similar to the second case and PA output power is same i.e. 5 dBm. However, in the third case, $M$ and $P$ are configured to generate the appropriate leakage cancellation signal to mitigate the effect of the TX leakage signal on the RX. It can be seen that in case (3) the signal is very similar to the case (1) as if there is no TX leakage signal.

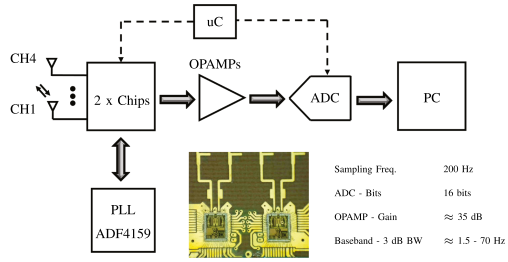


**FIGURE 23.** Preliminary radar prototype.

**TABLE 2.** Noise Measurement Cases

| Case | Description |
|---|---|
| Case A | LCCOFF + TXOFF |
| Case B | LCCON + TXOFF |
| Case C | LCCON + TXON (-9 dBm) |
| Case D | LCCON + TXON (-2 dBm) |
| Case E | LCCON + TXON (+4 dBm) |
| Case F | LCCOFF + TXON (+4 dBm) |

### D. PRELIMINARY RADAR MEASUREMENTS

Preliminary radar prototype was designed to determine the efficacy of the designed chips to measure the vital signs. Simplified block diagram of the radar prototype is shown in Fig. 23. Two RF chips are wire-bonded on the RF board and their oscillators work synchronously via the injection locking scheme [13]. External off-the-shelf phase lock loop (PLL) locks the phase of the oscillator with the phase of a precise external quartz oscillator. The PLL is also used to set the desired RF frequency of the chip for the CW radar operation i.e., 60 GHz. Each channel is connected to a 60 GHz on-board 4-element linear patch array antenna with the bond-wires. There is a bond-wire compensation network implemented to improve the RF matching. Channel 1 receiver IQ signals are connected to a 16-bit ADC after filtering and gain stages. The total baseband gain is 34 dB having 3-dB bandwidth from 1.5 Hz- 70Hz. The data is then sent to PC for plotting and analysis.

Fig. 24 shows the radar IQ signal for three different scenarios. The target in each scenario is a small corner reflector mounted on a linear stage with the speed of $\approx$0.65 cm/s having to and fro motion at a distance of 1 *m* from the radar. In the Bi-static scenario, CH1 TX is off; and, the signal is transmitted from CH2 and received from CH1. The TX to

**TABLE 3.** Performance Comparison Among State of the Art Leakage Cancellation Circuits

| Reference | Frequency $(GHz)$ | \| LC Depth \| $(dB)$ | Total Isolation $(dB)$ | LCC Area $(mm^2)$ | LCC Power Consumption $(mW)$ | TX Power $(dBm)$ | RX Gain $(dB)$ | RX $IP_{1dB}$ $(dBm)$ | LCC |
|---|---|---|---|---|---|---|---|---|---|
| MTT, 2016 [4] | 60 | 23.4 | 53 | 0.5 [g] | 21 | 3 | 10.5 | -23 | VGA + Phase Shifter |
| JSSC, 2021 [7] | 160 | – | 40 | 0.26 [g] | 66 | 3 | 24 | -18 | Vector Modulator |
| MTT, 2021 [10] | 79 | – | 44 [β] | 0.03 [g] | 0 | - | 31 | -14 | Digital Impedance Tuner (1) |
| ISSCC, 2019 [16] | 60 | – | 45 | 1.72 [γ] | 41 | - | - | - | - |
| This Work | 60 | 27 [α] | 49 | 0.04 | 4 (3) | 4.5 | 30 | -20 | Impedance Tuner (2) |

[α] 34 dB measured at 59.2 GHz.
[β] Using advanced control algorithm to overcome the limited resolution of digital Impedance Tuner.
[γ] Area of the complete coupler
[g] Graphically estimated
(1) **3.3-bit phase resolution (i.e. 10 phase states), 2-bit magnitude resolution**
(2) **5-bit phase resolution (i.e. 32 phase states), 8-bit magnitude resolution**
(3) Max. power consumption when $M = 255$.

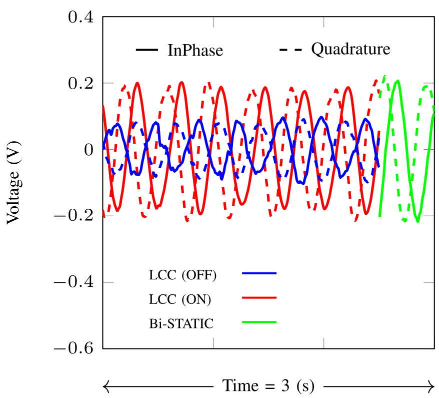


**FIGURE 24.** Measured radar IQ data with a 5 cm corner reflector (≈0 *dBsm* RCS) on a linear stage. Mono-static scenario with leakage cancellation system (LCC) ON/OFF is shown. For a comparison purpose, Bi-static scenario is also shown when signal is transmitted from Channel 2 and received from channel 1.

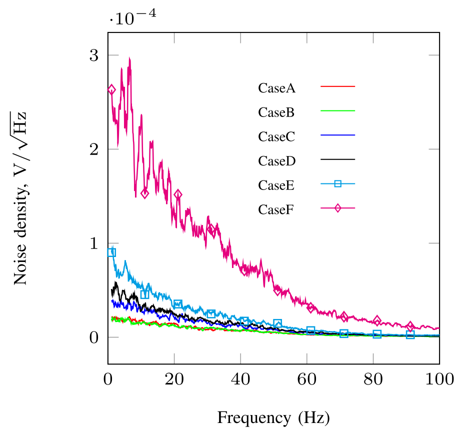


**FIGURE 25.** Measured voltage noise density of the radar signal after amplification (see Fig. 23) for different scenarios mentioned in Table 2.

RX isolation is very high because of different TX and RX channels. In the other two scenarios, the CH1 is being used as both TX and RX (i.e., mono-static radar). When LCC is OFF, the TX signal leaking into RX saturates the receiver. Coupler isolation is 22 dB at 60 GHz, RX $IP_{1dB}$ point is $-20$ dBm; so, 10 dBm output power from PA drives the RX into 8 dB saturation. However, when LCC is ON, it provides the additional isolation of 27 dB. TX leakage power at RX input becomes $\approx -39$ dBm i.e., much lower than the receiver $IP_{1dB}$, and IQ signal magnitude increases by 8 dB achieving the same value as that of Bi-static case. The LNA gain $G_{LNA}$ is limited to maximum 20 dB in the current chip version; however, $G_{LNA}$ can be further increased by 10 dB giving 10 dB more SNR according to Fig. 4, thanks to the LCC. Note that the requirement of the mixer $IP_{1dB}$ or LNA output 1-dB point $OP_{1dB}$ doesn't change with increasing $G_{LNA}$.

Fig. 25 shows the measured voltage noise density after the baseband amplification for the different scenarios mentioned in Table 2. Case A shows the measured noise density of the RX. Case B shows the noise density of the RX when LCC is also ON. Both the cases perfectly overlap with each other indicating that LCC doesn't increase the noise floor at the LNA input at 60 GHz as analyzed in Section III-D. Cases C, D and E show the measured noise density with the TX power when LCC is active. Case F shows the noise density when TX is on but LCC is deactivated. Ideally, the noise density shouldn't increase with the increasing TX power because phase noise of the TX signal (i.e., dominant TX noise source) is correlated to the RX LO signal for the short range radar. However, the TX amplitude noise has no correlation to the RX LO and it increases the RX noise floor if TX/RX isolation is limited [17]. Moreover, in the current chip version, on-chip power distribution network and grounding scheme need optimization. There is somewhat higher amplitude noise and AM-PM conversion in the TX section because of supply/GND ringing due to the bond-wire inductances.

## V. CONCLUSION

An ultra-compact impedance tuner (IT) having 5-bit phase resolution and 8-bit magnitude resolution has been designed and the design parameters have been explained in detail. IT is based on high impedance transmission line of length 527 $\mu$m and TAR cells which are based on SiGe transistors in the reverse saturated topology. It has been shown that the reverse saturated topology offers half the parasitic capacitance as compared to the standard topology and hence the phase resolution of the IT can be doubled. Very good leakage cancellation performance in the radar chip was proven in the measurements. The impedance tuner provides the leakage cancellation depth of 27 dB at 60 GHz. A comparison of current work to the state of the art is summarized in Table 3. The IT based leakage cancellation circuitry in this work is very compact and has a very low power consumption while providing high leakage cancellation depth at the same time; thanks to the 8-bit and 5-bit magnitude and phase resolution of the IT respectively. The IT circuit concept described can be used advantageously in many types of radar circuits.

## ACKNOWLEDGMENT

The authors would like to thank their colleagues S. Peter, N. Khail, A. Kasal and S. Glisic for the board design and assembly, and D. Genschow for providing the linear stage. Moreover, they would like to thank IHP for providing the measurement instruments.

## REFERENCES

[1] F.-K. Wang, J.-X. Zhong, and J.-Y. Shih, "IQ signal demodulation for noncontact vital sign monitoring using a CW Doppler radar: A review," *IEEE J. Electromagn., RF Microw. Med. Biol.*, vol. 6, no. 4, pp. 449–460, Dec. 2022, doi: 10.1109/JERM.2022.3214753.

[2] C. Will et al., "Radar-based heart sound detection," *Sci. Rep.*, vol. 8, 2018, Art. no. 11551, doi: 10.1038/s41598-018-29984-5.

[3] M. Kalantari, W. Li, H. Shirinabadi, A. Fotowat-Ahmady, and C. P. Yue, "A W-band single-antenna FMCW radar transceiver with adaptive leakage cancellation," *IEEE J. Solid-State Circuits*, vol. 56, no. 6, pp. 1655–1667, Jun. 2021, doi: 10.1109/JSSC.2020.3032677.

[4] H.-C. Kuo et al., "A fully integrated 60-GHz CMOS direct-conversion Doppler radar RF sensor with clutter canceller for single-antenna noncontact human vital-signs detection," *IEEE Trans. Microw. Theory Techn.*, vol. 64, no. 4, pp. 1018–1028, Apr. 2016, doi: 10.1109/TMTT.2016.2536600.

[5] C.-C. Chou, W.-C. Lai, Y.-K. Hsiao, and H.-R. Chuang, "60-GHz CMOS Doppler radar sensor with integrated V-band power detector for clutter monitoring and automatic clutter-cancellation in noncontact vital-signs sensing," *IEEE Trans. Microw. Theory Techn.*, vol. 66, no. 3, pp. 1635–1643, Mar. 2018, doi: 10.1109/TMTT.2017.2777467.

[6] X. Jiang, X. Gao, X. Wu, Q. J. Gu, and X. Liu, "Automatic RF leakage cancellation for improved remote vital sign detection using a low-IF dual-PLL radar system," *IEEE Trans. Microw. Theory Techn.*, vol. 71, no. 6, pp. 2664–2679, Jun. 2023, doi: 10.1109/TMTT.2022.3231658.

[7] M. Kucharski, W. A. Ahmad, H. J. Ng, and D. Kissinger, "Monostatic and bistatic G-band BiCMOS radar transceivers with on-chip antennas and tunable TX-to-RX leakage cancellation," *IEEE J. Solid-State Circuits*, vol. 56, no. 3, pp. 899–913, Mar. 2021, doi: 10.1109/JSSC.2020.3041045.

[8] M. Kucharski, D. Kissinger, and H. J. Ng, "A monostatic E-band radar transceiver with a tunable TX-to-RX leakage canceler for automotive applications," in *Proc. IEEE/MTT-S Int. Microw. Symp.*, Philadelphia, PA, USA, 2018, pp. 591–594, doi: 10.1109/MWSYM.2018.8439230.

[9] P. Fenske, A. Scheder, T. Koegel, K. Root, M. Vossiek, and C. Carlowitz, "Self-interference leakage estimation 'N' cancellation element: Design of an active self-interference cancellation coupler," *IEEE Microw. Mag.*, vol. 24, no. 6, pp. 68–75, Jun. 2023, doi: 10.1109/MMM.2023.3256380.

[10] M. Porranzl, C. Wagner, H. Jaeger, and A. Stelzer, "High-bandwidth quasi-circulator-based monostatic automotive radar with self-interference suppression," *IEEE Trans. Microw. Theory Techn.*, vol. 69, no. 1, pp. 198–209, Jan. 2021, doi: 10.1109/TMTT.2020.3036007.

[11] M. Porranzl, C. Wagner, H. Jaeger, and A. Stelzer, "A digital 70–140–GHz impedance tuner in 130-nm CMOS technology," in *Proc. Eur. Microw. Conf.*, Paris, France, 2015, pp. 1184–1187, doi: 10.1109/EuMC.2015.7345980.

[12] M.-Y. Huang and H. Wang, "An ultra-compact folded inductor based mm-Wave rat-race coupler in CMOS," in *Proc. IEEE MTT-S Int. Microw. Symp.*, San Francisco, CA, USA, 2016, pp. 1–4, doi: 10.1109/MWSYM.2016.7540119.

[13] A. Mushtaq, W. Winkler, and D. Kissinger, "A 79-GHz scalable FMCW MIMO automotive radar transceiver architecture with injection-locked synchronization," in *Proc. IEEE MTT-S Int. Microw. Symp.*, Boston, MA, USA, 2019, pp. 690–693, doi: 10.1109/MWSYM.2019.8700731.

[14] N. Rinaldi and M. Schröter, Eds., *Silicon-Germanium Heterojunction Bipolar Transistors for Mm-wave Systems Technology, Modeling and Circuit Applications*, 1st ed. Aalborg, Denmark: River Publishers, 2018, doi: 10.1201/9781003339519.

[15] R. L. Schmid, A. Ç. Ulusoy, P. Song, and J. D. Cressler, "A 94 GHz, 1.4 dB insertion loss single-pole double-throw switch using reverse-saturated SiGe HBTs," *IEEE Microw. Wireless Compon. Lett.*, vol. 24, no. 1, pp. 56–58, Jan. 2014, doi: 10.1109/LMWC.2013.2288276.

[16] A. Nagulu and H. Krishnaswamy, "28.5 non-magnetic 60 GHz SOI CMOS circulator based on loss/dispersion-engineered switched bandpass filters," in *Proc. IEEE Int. Solid-State Circuits Conf.*, San Francisco, CA, USA, 2019, pp. 446–448, doi: 10.1109/ISSCC.2019.8662467.

[17] H. Jaeger, M. Porranzl, H. Knapp, and E. Kolmhofer, "Amplitude noise measurement of an automotive 77-GHz VCO," in *Proc. IEEE MTT-S Int. Conf. Microw. Intell. Mobility*, San Diego, CA, USA, 2016, pp. 1–3, doi: 10.1109/ICMIM.2016.7533922.

**AHMAD MUSHTAQ** is currently a Principal RF Designer with Indie Semiconductor, Frankfurt, Germany. His research interests include cost effective mm-wave radar circuit design and optimization algorithms. He is also interested in contributing to the development of low cost/open-source design-flow ranging from radar chip design to system design, electromagnetic simulations and radar system behavioural modeling for various industrial and consumer applications.

**THOMAS MAUSOLF** received the Diploma in electrical and information technology from the University of Applied Science Brandenburg, Brandenburg an der Havel, Germany, in 2005. From 2006 to 2018, he was leading the Design Kit Group, IHP, developing various process design kits (PDK) for IHPs 0.25 and 0.13 µm high performance SiGe BiCMOS technologies. From 2018 to 2024, he had led the High Frequency Characterization Laboratory at IHP.

**WOLFGANG MIESCH** received the Dipl.-Ing. degree from Technische Hochschule Ilmenau, East Germany (GDR), in 1985. From 1985 to 1994, he was a Design Engineer for telecommunication IC especially for high voltage BCDMOS ICs with VEB Halbleiterwerk Frankfurt (Oder), GDR. From 1994 to 2016, he was a Senior Design Engineer for industrial HV ICs with alpha microelectronis GmbH, Germany. From 2016 to 2023, he was a System Engineer with the Silicon Radar GmbH Frankfurt (Oder), Germany. He is currently a Senior Analog IC Design Engineer with Indie Semiconductor, Frankfurt (Oder).

**NASIR UDDIN** (Member, IEEE) received the M.Sc. degree in electrical communication engineering from the University of Kassel, Kassel, Germany, in 2007, and the Ph.D. degree in electrical engineering from the University of Paderborn, Paderborn, Germany, in 2011. In 2011, he joined SSB GmbH, Germany, as a Research and Development Engineer. From 2012 to 2023, he was an RFIC Designer with Silicon Radar GmbH Frankfurt (Oder), Germany. He is currently a Senior RFIC Designer with Indie Semiconductor, Frankfurt (Oder). His research interests include integrated circuits for radar and sensor applications.

**WOLFGANG WINKLER** (Member, IEEE) received the M.S. and Ph.D. degrees in electrical engineering from Technical University Ilmenau, Ilmenau, Germany, in 1979 and 1984, respectively. From 1984 to 2007, he was a Researcher with the Leibniz Institute for High Performance Microelectronics, Frankfurt (Oder), Germany. He is the Founder and was the CTO of the company Silicon Radar GmbH, Frankfurt (Oder), from 2007 to 2020 and is currently a Manager Innovations with indie Semiconductor FFO GmbH. His research interests include integrated circuits for radar applications in silicon-based technologies. He designed integrated circuits for several radar-applications, e.g., for low-cost automotive, space, and industrial and consumer applications. He brought several innovative integrated circuit types to series production. Among others it is the first highly integrated 122 GHz ISM-band radar transceiver in SiGe BiCMOS technology that is in volume production since 2017. Dr. Winkler is a member of IEEE Microwave Theory and Technology Society.

**DIETMAR KISSINGER** (Fellow, IEEE) received the Dipl.-Ing., Dr.-Ing., and habil. degree in electrical engineering from FAU Erlangen-Nürnberg, Erlangen, Germany, in 2007, 2011 and 2014, respectively. From 2007 to 2010, he was with Danube Integrated Circuit Engineering, Linz, Austria, where he was a System and Application Engineer with the Automotive Radar Group. From 2010 to 2014, he was a Lecturer and the Head of the Radio Frequency Integrated Sensors Group, Institute for Electronics Engineering, Erlangen. From 2015 to 2018, he was with Technische Universität Berlin, Berlin, Germany, and the Head of the Circuit Design Department, IHP, Frankfurt (Oder). Since 2019, he has been a Full Professor of high-frequency circuit design with Ulm University, Ulm, Germany, and the Head of the Institute of Electronic Devices and Circuits. He has authored or coauthored more than 400 technical papers and holds more than ten patents. His research interests include silicon high-frequency and high-speed integrated circuits and systems for communication and automotive, industrial, security, and biomedical sensing applications. Dr. Kissinger has served on the technical program committees of the IEEE European Solid-State Circuits Conference, IEEE BiCMOS and Compound Semiconductor Integrated Circuits and Technology Symposium, IEEE MTT-S International Microwave Symposium (IMS), European Microwave Week (EuMW), Radio and Wireless Week (RWW), and German Microwave Conference (GeMiC). He was the two-time Chair of the IEEE Topical Conference on Wireless Sensors and Sensor Networks and IEEE Topical Conference on Biomedical Wireless Technologies, Networks and Sensing Systems. He was the TPC Chair of the 2022 GeMiC, as a member of the 2013 and 2017 EuMW Organizing Committee, as member of the 2018 IEEE MTT-S IMS Steering Committee, and as Executive Committee Chair of the RWW. He was the nine-time Guest Editor of the *IEEE Microwave Magazine* and was an Associate Editor for IEEE TRANSACTIONS ON MICROWAVE THEORY AND TECHNIQUES. He was the Chair of the IEEE MTT-S Technical Committee on Microwave and Millimeter-Wave Integrated Circuits (MTT-14) and is currently an elected member of the IEEE MTT-S Administrative Committee. He was the recipient of the 2017 IEEE MTT-S Outstanding Young Engineer Award, 2017 VDE/VDI GMM-Prize, 2018 VDE ITG-Prize, 2023 IEEE Microwave Prize, and was the co-recipient of more than ten best paper awards.